

HNC, HCN and CN in Seyfert galaxies[★]

J.P. Pérez-Beaupuits^{1,2}, S. Aalto², and H. Gerebro²

¹ Kapteyn Astronomical Institute, Rijksuniversiteit Groningen, 9700 AV Groningen, The Netherlands - e-mail: jp@astro.rug.nl

² Onsala Rymdobservatorium, Chalmers Tekniska Högskola, S - 439 92 Onsala, Sweden - e-mail: susanne@oso.chalmers.se

Received 14 August 2007 / Accepted 27 September 2007

ABSTRACT

Aims. Bright HNC 1–0 emission, rivalling that of HCN 1–0, has been found towards several Seyfert galaxies. This is unexpected since traditionally HNC is a tracer of cold (10 K) gas, and the molecular gas of luminous galaxies like Seyferts is thought to have bulk kinetic temperatures surpassing 50 K. There are four possible explanations for the bright HNC: (a) Large masses of hidden cold gas; (b) chemistry dominated by ion-neutral reactions; (c) chemistry dominated by X-ray radiation; and (d) HNC enhanced through mid-IR pumping. In this work we aim to distinguish the cause of the bright HNC and to model the physical conditions of the HNC and HCN emitting gas.

Methods. We have used SEST, JCMT and IRAM 30m telescopes to observe HNC 3–2 and HCN 3–2 line emission in a selection of 5 HNC-luminous Seyfert galaxies. We estimate and discuss the excitation conditions of HCN and HNC in NGC 1068, NGC 3079, NGC 2623 and NGC 7469, based on the observed 3–2/1–0 line intensity ratios. We also observed CN 1–0 and 2–1 emission and discuss its role in photon and X-ray dominated regions.

Results. HNC 3–2 was detected in 3 galaxies (NGC 3079, NGC 1068 and NGC 2623). Not detected in NGC 7469. HCN 3–2 was detected in NGC 3079, NGC 1068 and NGC 1365, it was not detected in NGC 2623. The HCN 3–2/1–0 ratio is lower than 0.3 only in NGC 3079, whereas the HNC 3–2/1–0 ratio is larger than 0.3 only in NGC 2623. The HCN/HNC 1–0 and 3–2 line ratios are larger than unity in all the galaxies. The HCN/HNC 3–2 line ratio is lower than unity only in NGC 2623, which makes it comparable to galaxies like Arp 220, Mrk 231 and NGC 4418.

Conclusions. We conclude that in three of the galaxies the HNC emissions emerge from gas of densities $n \lesssim 10^5 \text{ cm}^{-3}$, where the chemistry is dominated by ion-neutral reactions. The line shapes observed in NGC 1365 and NGC 3079 show that these galaxies have no circumnuclear disk. In NGC 1068 the emission of HNC emerges from lower ($< 10^5 \text{ cm}^{-3}$) density gas than HCN ($> 10^5 \text{ cm}^{-3}$). Instead, we conclude that the emissions of HNC and HCN emerge from the same gas in NGC 3079. The observed HCN/HNC and CN/HNC line ratios favor a PDR scenario, rather than an XDR one, which is consistent with previous indications of a starburst component in the central regions of these galaxies. However, the $N(\text{HNC})/N(\text{HCN})$ column density ratios obtained for NGC 3079 can be found only in XDR environments.

Key words. galaxies: ISM — galaxies: starburst — galaxies: active — galaxies: Seyfert — radio lines: galaxies — radio lines: ISM

1. Introduction

The hydrogen cyanide, HCN molecule, is commonly used as an extragalactic tracer of molecular gas with densities $n(\text{H}_2)$ larger than 10^4 cm^{-3} (e.g. Solomon et al. 1992; Curran et al. 2000; Kohn 2005). The HCN to CO intensity ratio varies significantly, from 1/3 to 1/40 in starburst galaxies, and it has not been determined whether this variation depends on the dense molecular gas content or on the abundance and/or excitation conditions. In addition, recent results seems to indicate that HCN may not be an unbiased tracer of the dense molecular gas content in LIRGs and ULIRGs (Graciá-Carpio et al. 2006). It is essential, therefore, to use other molecular tracers than HCN, in order to understand the physical conditions in the dense gas.

A molecule of particular interest, for comparison with HCN, is its isomer HNC. The detection of interstellar HNC supports the theory of dominant ion-molecule chemistry in dark molecular clouds. Both species are thought to be created by the same dissociative recombination of HCNH^+ . This ion can produce HCN and HNC, with approximately equal abundances. Models

based only on this scheme would predict then an HNC/HCN ratio ≈ 1 . However, the observed HNC/HCN abundance ratios vary significantly between different kinds of molecular clouds - the ratio ranges from 0.03 to 0.4 in warm cores ($T_k > 15 \text{ K}$), and can be as high as 4.4 in cold cores ($T_k < 15 \text{ K}$).

The CN (cyanogen radical) molecule is another tracer of dense gas, with a lower (by a factor of 5) critical density than HCN. CN is also chemically linked to HCN and HNC by photodissociations (e.g. Hirota & Yamamoto 1999). Surveys of the 1–0 transition of CN and HNC have been done in order to trace a cold, dense phase of the gas in luminous galaxies (Aalto et al. 2002). It was found that the HNC 1–0 luminosities often rivalled those of HCN 1–0. These results seem to contradict the idea of warm ($T_k \gtrsim 50 \text{ K}$) gas in the centers of luminous galaxies (e.g. Wild et al. 1992; Wall et al. 1993) whose IR luminosities were suggested to originate from star formation rather than AGN activity (Solomon et al. 1992).

According to observations in the vicinity of the hot core of Orion KL, experimental data, chemical steady state and shock models, the HNC/HCN ratio decreases as the temperature and density increase (e.g. Schilke et al. 1992; Talbi et al. 1996; Tachikawa et al. 2003). If a bright HNC 1–0 transition line is nevertheless detected under these conditions, it could be due to the following possible explanations: (a) the presence

Send offprint requests to: J.P. Pérez-Beaupuits

[★] Research supported by the Swedish Institute as a scholarship granted to J.P. Pérez-Beaupuits to pursue his M.Sc. degree at Chalmers Tekniska Högskola, Sweden

Table 1. Sample of galaxies ^a.

Galaxy	Seyfert	RA [hh mm ss]	DEC [° ' "]	v_{sys} [km s ⁻¹]	Distance ^b [Mpc]	$\Omega_S(\text{CO})$ ^c [" ²]	$\Omega_S(\text{HCN})$ ^d [" ²]
NGC 3079	2	10 01 57.805	+55 40 47.20	1116±1	15.0±1.1	15 × 7.5	5 × 5
NGC 1068	2	02 42 40.711	-00 00 47.81	1137±3	15.3±1.1	30 × 30	10 × 10
NGC 2623	2	08 38 24.090	+25 45 16.80	5549±1	74.6±5.4	8 × 8	2.6 × 2.6
NGC 1365	1.8	03 33 36.371	-36 08 25.45	1636±1	22.0±1.6	50 × 50	16.5 × 16.5
NGC 7469	1.2	23 03 15.623	+08 52 26.39	4892±2	65.8±4.8	8 × 8	4 × 6

- a) The Seyfert classification, positions (in equatorial J2000 coordinates) and heliocentric radial velocities were taken from NED.
b) The distances were calculated using the Hubble constant ($H_0 \approx 74.37 \text{ km s}^{-1} \text{ Mpc}^{-1}$) estimated by Ngeow and Kanbur (2006).
c) The source sizes of the CO 1–0 transition line were estimated from the maps presented in (Koda et al. 2002) for NGC 3079, (Schinnerer et al. 2000) for NGC 1068, (Bryant et al. 1999) for NGC 2623, (Sandqvist 1999) for NGC 1365, and (Papadopoulos & Allen 2000) for NGC 7469. The source sizes for the $J = 2 - 1$ transition line were assumed equal to that of the $J = 1 - 0$ line. For NGC 7469, the source size of the CO 2–1 emission estimated from the corresponding map presented by Davies et al. (2004) agrees well with the source size estimated for the CO 1–0 line.
d) Source sizes of HCN 1–0 were estimated from the corresponding maps published in (Kohno et al. 2000) for NGC 3079, (Kohno et al. 2001 and Helfer & Blitz 1995) for NGC 1068, (Davies et al. 2004) for NGC 7469. The source sizes of NGC 2623 and NGC 1365 were estimated using proportions found in NGC 1068 (read text in §3.5). Because of their chemical link, the source sizes of the CN and HNC molecules were assumed the same as that of HCN. Due to the lack of high resolution maps, the source sizes corresponding to the emission of the higher transition lines were assumed equal to that of the $J = 1 - 0$ line.

of large masses of hidden cold gas and dust at high densities ($n > 10^5 \text{ cm}^{-3}$); (b) chemistry dominated by ion-molecule reactions with HCNH^+ at low density ($n \approx 10^4 \text{ cm}^{-3}$) in regions where the temperature dependence of the HNC abundance becomes weaker; (c) enhancement by mid-IR pumping, also in low density regions where the lines would not be collisionally excited; and (d) the influence of UV-rays in Photon Dominated Regions (PDRs) and/or X-rays in X-ray Dominated Regions (XDRs) at densities $n \gtrsim 10^4 \text{ cm}^{-3}$ and at total column densities $N_{\text{H}} > 3 \times 10^{21} \text{ cm}^{-2}$ (Meijerink & Spaans 2005).

In the case of CN, observations of its emission towards the Orion A molecular complex (Rodríguez-Franco et al. 1998) suggest that this molecule is also enhanced in PDRs, but particularly in XDRs, where a CN/HCN abundance ratio larger than unity is expected (e.g., Lepp & Dalgarno 1996 and Meijerink, Spaans, Israel 2007).

We have observed low and high transition lines of the HCN, HNC and CN molecules in a group of Seyfert galaxies, which are supposed to host both sources of power, AGN and starburst activity, in their central region. Our interest is to assess the excitation conditions of HCN and HNC, distinguish between the above possible causes of the bright HNC, and to explore the relation between the CN emission, XDRs and dense PDRs in these sources.

In §2 we describe the observations. The results (spectral lines, line intensities and line ratios) are presented in §3. The interpretation of line shapes and gas distribution in the most relevant cases, as well as the possible explanations for the bright HNC and the modelling of the excitation conditions of HCN and HNC are discussed in §4. The conclusions and final remarks of this work are presented in §5.

2. Observations

We have used the James Clerk Maxwell Telescope (JCMT) in 2005 to observe the HNC $J=3-2$ (271 GHz) and the HCN $J=3-2$ (267 GHz) lines towards a sample of Seyfert galaxies. Observations of CN and HNC $J=1-0$ (90 GHz) were made in 2002 using the Swedish ESO Southern Telescope (SEST). HCN $J=1-0$ (88 GHz) data from literature were also used. The system temperatures ranged between 350 K and 430 K. In the case of

Table 2. Beamsizes & efficiencies.

Transition	ν [GHz]	HPBW ^a ['']	η_{mb} ^a	Telescope ^a
HCN 1-0	88.632	44 28	0.65 0.77	OSO IRAM
HNC 1-0	90.663	55 27	0.74 0.77	SEST IRAM
CN 1-0	113.491	45 22	0.71 0.74	SEST IRAM
CO 1-0	115.271	44 21	0.70 0.74	SEST IRAM
CN 2-1	226.875	23 11	0.51 0.53	SEST IRAM
CO 2-1	230.538	20 11	0.66 0.52	JCMT IRAM
HCN 3-2	265.886	18 9	0.60 0.45	JCMT IRAM
HNC 3-2	271.981	18 9	0.60 0.44	JCMT IRAM

- a) The columns are divided in two sub-columns (*left*: OSO, SEST, JCMT, and *right* IRAM) indicating the telescope used to obtain the corresponding parameter. The IRAM 30m telescope was used to observe NGC 3079. The other sources were observed with the OSO 20m, SEST and JCMT telescopes.

CN $J=1-0$ (226 GHz) the weather conditions were not so good, making the system temperature range between 490 K and 760 K. Pointing was checked regularly on SiO masers and the rms was found to be about 3".

For the SEST observations we alternated between a 500 MHz and 1 GHz backend, depending on weather. Simultaneous observations with the 1 and 3 mm receiver were taking place. In addition, the data of the Seyfert galaxy NGC 3079 obtained during the IRAM survey in 2006 is included in this work. We used the software package XS (written by P. Bergman) to reduce the data and fit the gaussians. Beamsizes and efficiencies are shown in Table 2.

The sample consists of five Seyfert galaxies of which two are Seyfert 1 type and three are considered mainly Seyfert 2. Table 1 lists the coordinates of the center positions observed in these galaxies, their sub-classification as Seyfert galaxies and heliocentric radial velocities, according to the NASA/IPAC Extragalactic Database (NED) (<http://nedwww.ipac.caltech.edu/>). The distances were calculated assuming a Hubble constant of $H_0 = 74.37 \pm 2.27 \text{ km s}^{-1} \text{ Mpc}^{-1}$ (Ngeow and Kanbur, 2006).

3. Results

3.1. NGC 1068

The molecular line emissions observed in NGC 1068 are shown in Figure 1. A first-order polynomial was used in most cases to correct the baselines, with the exception of the HCN 3–2 and CN 2–1 spectra, for which a second-order polynomial was required. The velocity resolution was set to 15 km s^{-1} for CO and CN, whereas a 25 km s^{-1} resolution was used for HNC and HCN. These velocity resolutions represent less than 10% of the line widths. The spectra are centered with respect to the heliocentric systemic velocity $v_{\text{sys}} = 1137 \text{ km s}^{-1}$ (from NED).

The $J=1-0$ and $J=2-1$ lines of CO show a triple structure where the peaks can be attributed mainly to the bars and the spiral arms, as described by Helfer & Blitz 1995.

We detect two of the main spingroups of CN 1–0: the 1–0 ($J = 3/2 - 1/2$, $F = 5/2 - 3/2$) line at the center of the spectrum, and the 1–0 ($J = 1/2 - 1/2$, $F = 3/2 - 3/2$) line shifted 856 km s^{-1} to the right. This spectrum shows three components as well, however they are hard to distinguish due to the blending. In fact if we freely fit three gaussian components, the uncertainties of the center velocity, amplitude and line width are about 100% or larger. Instead, if we set the line width of the central component to 154 km s^{-1} , which corresponds to the line width found for the CN $J=2-1$ line as described below, we get reasonable values. Only the first gaussian component shows high uncertainties in the amplitude and line width. Since the beam sizes of the CN and CO molecules are similar at the frequencies of the $J=1-0$ lines, we think that both beams pick up emission coming from the spiral arms and bars. Although, the nuclear region seems to be the predominant component in the case of CN.

Table 3. NGC 1068 line parameters.

Transition	Gaussian Component	V [km s^{-1}]	T_A^* [mK]	ΔV [km s^{-1}]
CO 1-0	1	1007 ± 1	225.2 ± 14.9	58 ± 3
	2	1100 ± 3	265.1 ± 3.8	156 ± 11
	3	1234 ± 2	215.3 ± 10.8	96 ± 4
CO 2-1	1	1007 ± 2	206.8 ± 32.5	63 ± 9
	2	1121 ± 4	529.3 ± 8.8	179 ± 16
	3	1245 ± 3	222.7 ± 37.8	81 ± 10
CN 1-0	1	1001 ± 23	12.8 ± 13.2	94 ± 42
	2	1091 ± 68	19.4 ± 4.7	154^a
	3	1213 ± 32	15.6 ± 9.5	136 ± 54
	4	1946 ± 26	8.3^b	154^a
CN 2-1	1	1093 ± 9	10.4 ± 0.9	154 ± 66
	2	1289 ± 14	6.2 ± 0.9	154^a
HCN 3-2	1	1103 ± 7	48.7 ± 2.4	275 ± 17
HNC 1-0	1	1073 ± 13	9.7 ± 1.8	114 ± 30
	2	1268 ± 20	6.7 ± 1.5	170 ± 62
HNC 3-2	1	1071 ± 9	12.9 ± 1.8	134 ± 23
	2	1250 ± 24	3.7 ± 2.5	70 ± 58

^a The line widths were set to the value found in the main component of the CN 2–1 line.

^b In order to avoid the effect of the artefact in the backend, the intensity was locked to the value expected for this spingroup.

Due to the second spingroup is corrupted by noise in the backend, we set the amplitude of the gaussian to 8.3 mK , which corresponds to the expected factor of about 0.43 times the amplitude of the main spingroup, according to the National Institute of Standards and Technology (NIST). The resulting central velocity of the second component was 1946 km s^{-1} ($\sim 113.169 \text{ GHz}$), i.e., about 22 MHz shifted from the expected frequency for this spingroup.

In the CN 2–1 line, the two spingroups at 226.8746 GHz ($2-1$, $J = 5/2 - 3/2$, $F = 7/2 - 5/2$) and 226.6596 GHz ($2-1$, $J = 3/2 - 1/2$, $F = 5/2 - 3/2$) are severely blended since the shift is $\sim 300 \text{ km s}^{-1}$. In order to identify the two spingroups we first fit two gaussian components to get the line width of the main spingroup, which is 154 ± 66 . We then set this value to both gaussian components and fit again the other parameters. The second spingroup is, in the optically thin limit, a factor 0.54 weaker than the main spingroup. We get a factor ~ 0.6 between the intensities obtained from the gaussian fit. On the other hand, the resulting center velocity of the second component is 1289 km s^{-1} , which corresponds to a shift of about 68 MHz with respect to the expected frequency of the second spingroup. Besides the noise in the data, this shift may also be produced by the influence of the unresolved spingroups, ($2-1$, $J = 3/2 - 1/2$, $F = 1/2 - 1/2$) and ($2-1$, $J = 3/2 - 1/2$, $F = 3/2 - 1/2$), located in between the two main spingroups. Together, these inter-spingroups would produce an intensity comparable to that of the second spingroup.

The line shape and intensity of the CN 2–1 spectrum differs from the one obtained by Usero et al. 2004 (thereafter U04). Besides the lack of baseline coverage observed in the U04 spectrum, there is a substantial discrepancy between the estimated source sizes. In U04 the emission of most of the molecules was assumed to emerge from a $6'' \times 4''$ region, which corresponds to their estimate of the size of the circumnuclear disk (CND), based

Table 4. NGC 1365 line parameters.

Transition	Gaussian Component	V [km s^{-1}]	T_A^* [mK]	ΔV [km s^{-1}]
CO 1-0	1	1532 ± 2	322.7 ± 5.2	136 ± 4
	2	1709 ± 3	260.3 ± 5.0	142 ± 5
CN 1-0	1	1511 ± 13	16.8 ± 3.5	130 ± 25
	2	1685 ± 33	8.9 ± 1.4	212 ± 92
	3	2356 ± 18	4.7 ± 1.2	130^a
CN 2-1	1	1526 ± 11	10.4 ± 1.5	130^a
	2	1727 ± 35	8.4 ± 1.9	212^b
	3	1846 ± 35	4.11 ± 3.5	130^a
HCN 3-2	1	1534 ± 5	51.4 ± 3.4	136 ± 13
	2	1706 ± 25	11.4 ± 3.3	142^c
HNC 1-0	1	1539 ± 11	16.0 ± 1.7	142 ± 23
	2	1750 ± 34	5.1 ± 1.4	195 ± 98

^a The two spingroups are supposed to have the same line width, so these were set according to the value found for the main spingroup of the CN 1–0 line.

^b The line width of the second component of the double peak structure was set to the corresponding value found in the CN 1–0 line.

^c The second component of HCN 3–2 seems to be affected by noise, so its line width was locked at $\Delta V = 142 \text{ km s}^{-1}$, i.e., the corresponding line width of the CO 1–0 line.

Table 5. NGC 3079 line parameters.

Transition	Gaussian Component	V [km s ⁻¹]	T_A^* [mK]	ΔV [km s ⁻¹]
CO 1-0	1	932± 4	129.4±11.8	143± 9
	2	1146± 3	374.3± 3.3	269±13
	3	1312± 6	145.1±13.1	74± 9
	4	1389± 5	186.3± 9.1	72± 5
CO 2-1	1	964±15	233.3±18.9	175±18
	2	1062±18	224.3±84.9	98±18
	3	1160±20	321.7±35.3	126±20
	4	1311±14	428.3± 9.4	190± 7
CN 1-0	1	967± 9	5.6± 0.6	162±23
	2	1287±15	4.5± 0.6	215±33
CN 2-1	1	997±14	8.1± 1.5	137±34
	2	1251±25	5.3± 1.3	203±69
HCN 1-0	1	1005±30	9.7± 1.4	249±73
	2	1274±21	10.7± 1.7	188±49
HCN 3-2	1	1033±42	6.4± 2.1	176±93
	2	1287±32	10.4± 1.8	219±70
HNC 1-0	1	983±17	6.5± 1.7	129±41
	2	1236±21	7.8± 1.5	157±38
HNC 3-2	1	996±48	7.4± 3.2	178±124
	2	1197±43	7.5± 3.8	120±90

on the CO 2–1 high resolution map presented by Schinnerer et al. (2000).

If we correct the peak antenna temperature ($T_A^* \approx 9.7$ mK) of our CN 2–1 spectrum, in order to obtain the main beam brightness temperature T_{mb} in the same way done in U04 ($T_{mb} = T_A^* \times \eta_{mb}^{-1} \times \Omega_{mb} \times \Omega_S^{-1}$), we get a peak T_{mb} of about 0.42 K, which is about 0.18 K (or a factor of ~ 1.8) larger than the peak temperature obtained by U04.

Due to the chemical link between HCN and CN, here we rather estimate the source size based on the high resolution map of HCN 1–0, published in Helfer & Blitz (1995). We estimate that the emissions of HCN, CN (and very likely HNC as well) emerge from a more extended region of about $10'' \times 10''$. This source size can also be inferred from the HCN 1–0 map presented by Kohno et al. (2001).

By correcting the peak antenna temperature (as described in §3.5) we get a peak T_{mb} of about 0.12 K, which is a factor 2 smaller than what was found by U04.

The HCN 3–2 line has its center velocity at $V \approx 1103$ km s⁻¹ which coincides with the main HCN emission shown in the position-velocity (p - v) map by Tacconi et al. (1994) (this is discussed in §4). The line width and line shape of this spectrum are consistent with HCN 1–0 spectra published in previous work (Nguyen-Q-Rieu et al. 1992, Curran et al. 2000).

The HNC spectra present a double peak profile in which the main peak has its center velocity at $V \approx 1070$ km s⁻¹ in both the $J=1-0$ and $J=3-2$ transitions. However, the line shape and intensity of the HNC 1–0 spectrum differs from the one obtained by Hüttemeister et al. (1995). The HNC 3–2 spectrum seems to be affected by noise, since the amplitude and line width of the secondary component have uncertainties larger than 50%. The different line shapes observed between the HNC and HCN

Table 6. Line parameters of NGC 2623 and NGC 7469. The third column indicate the gaussian components (G.C.) used to fit the spectral lines.

Source	Transition	G.C.	V [km s ⁻¹]	T_A^* [mK]	ΔV [km s ⁻¹]
N2623	HNC 3-2	1	5465±34	3.4± 0.7	337±88
N7469	CO 2-1	1	4773±0	0.15± 0	126±0
		2	4927±0	0.16± 0	123±0

spectra would indicate that they emerge from regions of different kinematics. The line parameters are summarized in Table 3.

3.2. NGC 1365

Figure 2 shows the molecular line emissions observed in NGC 1365. Without considering the second spingroups of CN, all the molecular spectra of NGC 1365 present a double peak structure, irrespective of the beam size or line transition.

This double peak structure can also be seen in the CO 2–1 and CO 3–2 spectra showed in Sandqvist et al. (1995) and in Sandqvist (1999), respectively.

The two strongest spingroups of the CN 1–0 line are also detected in this galaxy, with a double peak structure at the nuclear region. The strongest peak was used as reference for the main spingroup. We first fit two gaussian components to the main group and then we set the line width of the second spingroup, observed at around 2400 km s⁻¹, to the value found for the main spingroup. The proportion found between the amplitude of the spingroups is about 0.3 instead of the expected value of 0.43, according to NIST. The data around the second spingroup are strongly affected by noise, so its central velocity is shifted by about 50 km s⁻¹ from the expected value of about 800 km s⁻¹.

In the CN 2–1 line, the second spingroup overlaps with the double structure itself. The line widths of the two spingroups are set according to the value found for the CN 1–0 line. Given their combined intrinsic line strengths, the integrated line intensity ratio of the two spingroups is expected to be about 1.85 (assuming optically thin emission). If we also set the line width of the second peak of the double structure at 212 km s⁻¹, as found for CN 1–0, we get a proportion of about 0.4 between the two spingroups. Instead, if we set the amplitude of the second spingroup to 5.7 mK (the expected proportion) and we fit the line width of the double peak structure, we get a value of 181 km s⁻¹, which is about 30 km s⁻¹ less than the width found in the CN 1–0 line. In any case, the center velocity of the second spingroup is shifted by about 30 km s⁻¹ more than the expected velocity.

The HNC 1–0 and HCN 3–2 spectra have a structure similar to that of the CN 1–0 spectrum. Note that in CO 1–0 the double-peak is more pronounced than in the CN, HCN or HNC spectra, where the low velocity peak dominates. The line parameters are summarized in Table 4.

3.3. NGC 3079

The molecular line emissions observed in NGC 3079 are shown in Figure 3. The spectra are centered with respect to the heliocentric systemic velocity $v_{sys} = 1116$ km s⁻¹. The velocity resolution was set to 20 km s⁻¹ for HNC and HCN, and to 10 km s⁻¹ for CO and CN. Four structures are observed in the CO lines, which are not present in the other spectra. The CO lines are picking up

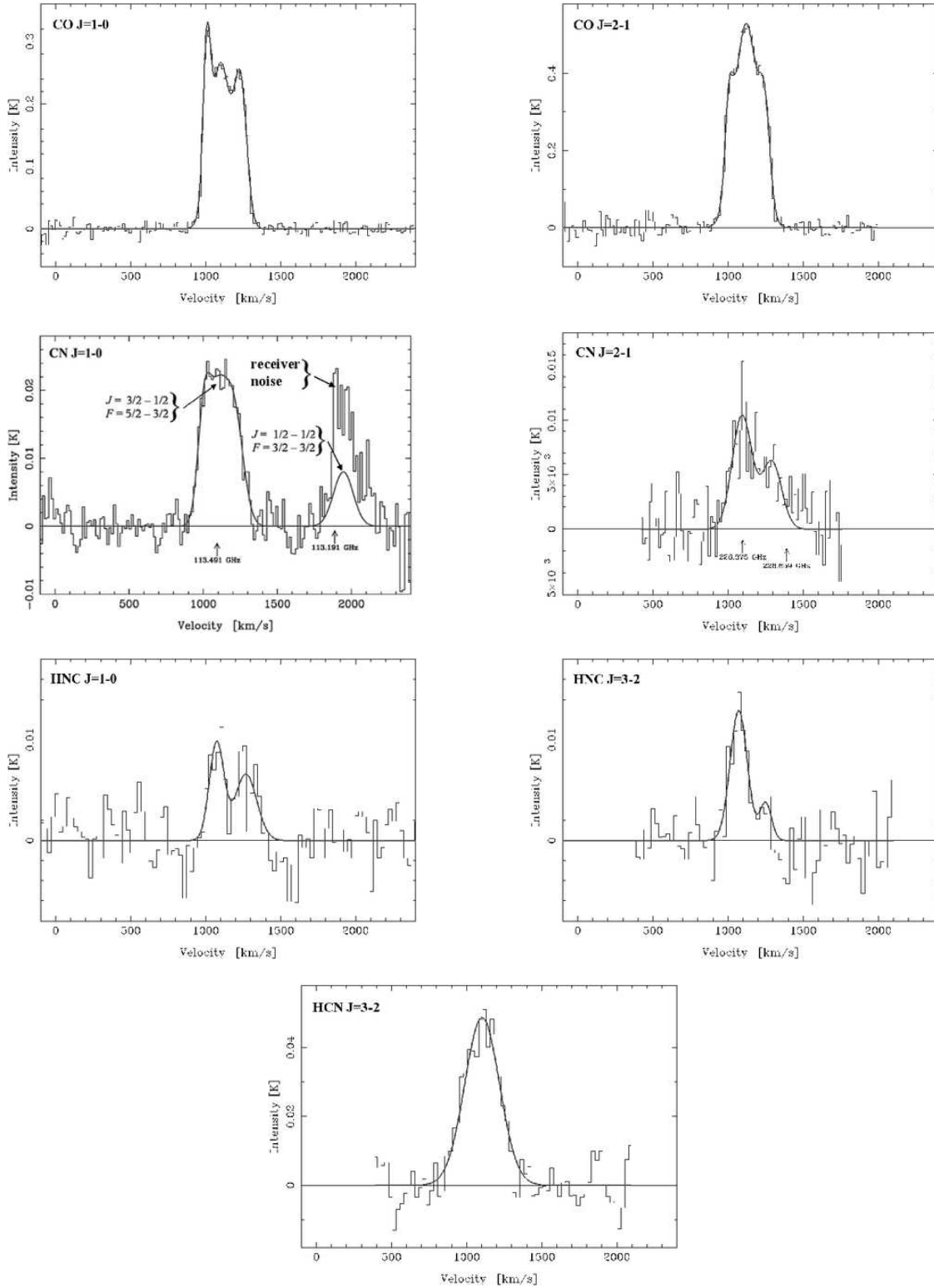


Fig. 1. Molecular line emissions in **NGC 1068**. The velocity resolution was set to 25 km s^{-1} for HNC and HCN, and to 15 km s^{-1} for CO and CN. The spectra are centered with respect to the heliocentric systemic velocity $v_{\text{sys}} = 1137 \text{ km s}^{-1}$. Emission from the spiral arms are detected in the CO 1-0 line. The CO 2-1 line is dominated by the emission coming from the CND. The two main spingroups of CN are detected in both $J=1-0$ and $J=2-1$ transitions. In the CN 1-0 the second spingroup is corrupted by noise in the spectrum. The two spingroups are blended in the CN 2-1 line. The different line shapes (profiles) of the HCN and HNC spectra seem to indicate that their emissions emerge from different regions.

extended lower density gas, compared to the CN lines (which have similar beam size). Hence the difference in line shape.

The CN 1-0 line present a double peak structure. Only the main spingroup ($J = 3/2 - 1/2$, $F = 5/2 - 3/2$) of the CN 1-0 line is

observed since the second spingroup falls beyond the bandwidth of the backend. In the CN 2-1 line, the two main spingroups, ($J = 5/2 - 3/2$, $F = 7/2 - 5/2$) and ($J = 3/2 - 1/2$, $F = 5/2 - 3/2$), are detected. But they are severely blended and merged with the

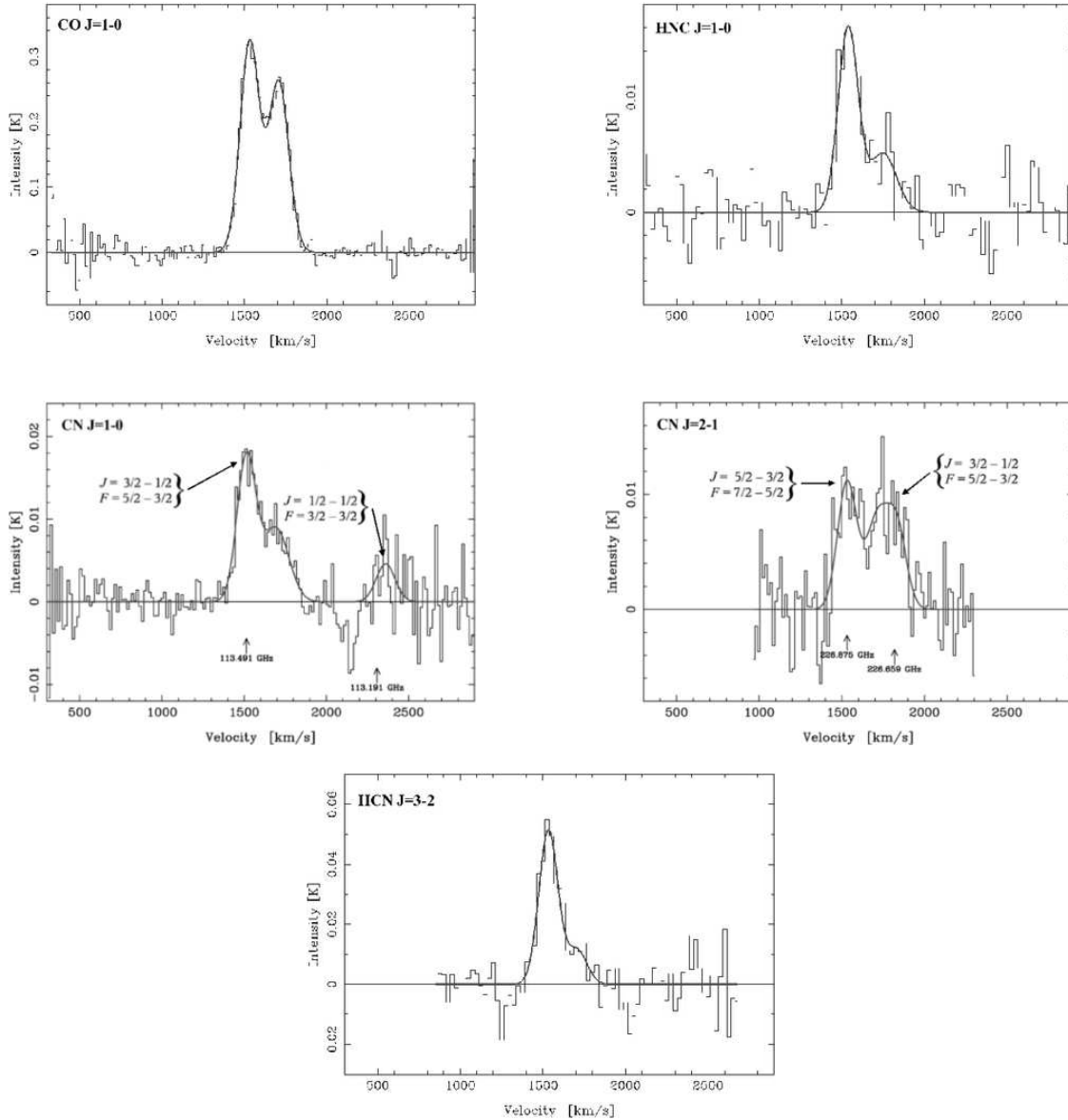


Fig. 2. Molecular line emissions in NGC 1365. The spectra are centered with respect to the heliocentric systemic velocity $v_{\text{sys}} = 1636 \text{ km s}^{-1}$. The velocity resolution was set to 25 km s^{-1} for HNC and HCN, and to 15 km s^{-1} for CO and CN. A double peak line shape is observed in all the spectra. This structure is related with the double peak emission coming from the center of the galaxy. In the CN spectra both spingroups are detected. The second spingroup of the CN 2–1 line overlaps the double structure itself.

double peak structure. In this case, only two gaussians were fitted because a third (middle) component presented large uncertainties in both the amplitude and line width, due to the noise in the spectrum. The two components are separated by only 254 km s^{-1} , and the proportion between their amplitudes is about 0.65. The difference between these and the expected values is attributed to the noise and the blending of the emission of the second spingroup.

The HCN spectrum of the $J=1-0$ and $J=3-2$ transitions agree with the HCN 1–0 spectrum obtained by Nguyen-Q-Rieu et al. (1992).

The HNC 1–0 spectrum is different from the tentative detection presented by Hüttemeister et al. (1995), which is broader and more intense than the spectrum showed here. Besides the similar line shapes, our HCN and HNC spectra extends from 900 km s^{-1} to 1300 km s^{-1} . Instead, the HNC spectrum showed in Hüttemeister et al. (1995) peaks at around 1300 km s^{-1} . Hence, we believe that our HNC detections are correct. In this case, be-

cause of the similar line shapes and widths (although the HNC 3–2 line is strongly affected by noise, and its peak intensities have uncertainties between 40% and 50%), the HCN and HNC emissions are likely emerging from the same gas. The line parameters are summarized in Table 5.

3.4. NGC 2623 and NGC 7469

The HNC 3–2 line emission observed in NGC 2623 is shown in the *left top panel* of Figure 4. The velocity resolution was set to 25 km s^{-1} . The spectrum is centered with respect to the heliocentric systemic velocity $v_{\text{sys}} = 5535 \text{ km s}^{-1}$ (NED). After a total integration time of 2 hours we do not detect HCN 3–2 emission in this galaxy.

The *right top panel* of Figure 4 shows the CO 2–1 spectrum observed in NGC 7469. The velocity resolution was set to 15 km s^{-1} . The spectrum is centered with respect to the systemic

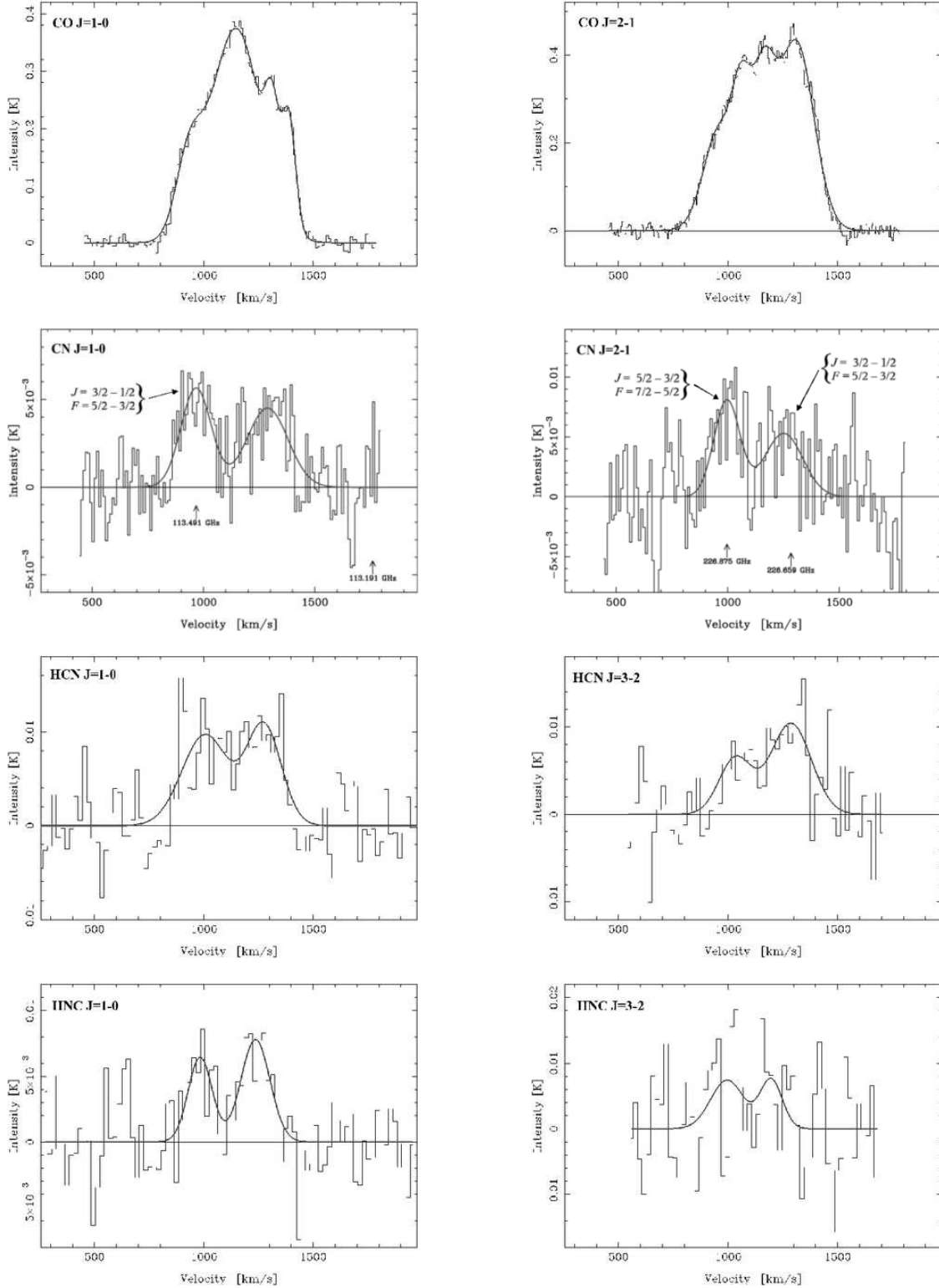


Fig. 3. Molecular line emissions in **NGC 3079**. The velocity resolution was set to 20 km s^{-1} for HNC and HCN, and to 10 km s^{-1} for CO and CN. The spectra are centered with respect to the heliocentric systemic velocity $v_{\text{sys}} = 1116 \text{ km s}^{-1}$. Emission from four structures are observed in the CO lines. Only the main spingroup is observed in the CN 1–0 line. The second spingroup is on the right edge of the spectrum, out of the bandwidth. Instead, both spingroups are observed in the CN 2–1 line, although the second spingroup overlaps the double structure of the CN emission. The both transitions of HCN and HNC have similar line shapes, which indicates that their emissions emerge from the same region.

velocity $v_{\text{sys}} = 4892 \text{ km s}^{-1}$. The CO spectrum shows a double peak structure, like the one observed in NGC 1365. We observed the HNC 3–2 line for about 1 hour of integration time, but we

do not detect any emission. The *bottom panels* show the spectra of the not detected lines. The line parameters of the detected transition lines are summarized in Table 6.

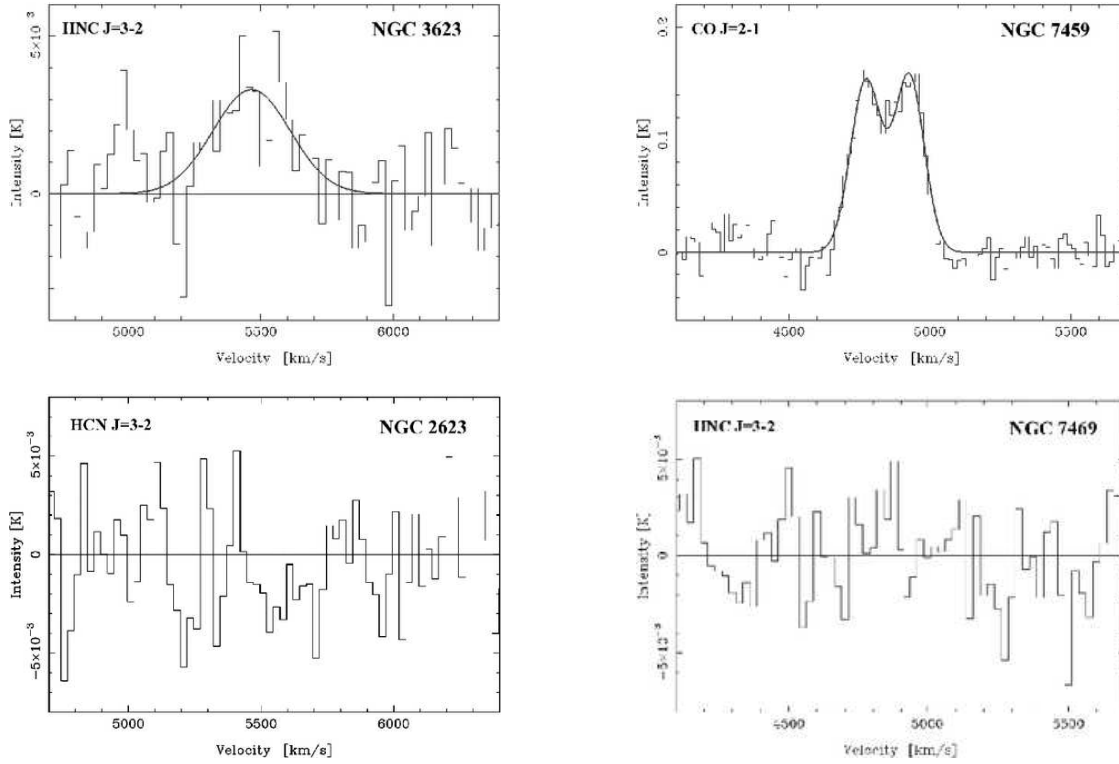


Fig. 4. Molecular line emissions in NGC 2623 (left) and NGC 7469 (right). The velocity resolution was set to 25 km s^{-1} for HNC and to 15 km s^{-1} for CO. The spectra are centered with respect to the heliocentric systemic velocities $v_{\text{sys}} = 5535$ and $v_{\text{sys}} = 4892 \text{ km s}^{-1}$ for NGC 2623 and NGC 7469, respectively. We do not detect HCN 3-2 emission in NGC 2623 nor HNC 3-2 in NGC 7469. Their observed intensities were less than 2σ .

3.5. Line intensities and ratios

The velocity integrated intensities are showed in Table 7. In order to compute the line intensity ratios were corrected for the different beam sizes obtained with different frequencies and telescopes, according to the correction factors defined for compact sources in Rohlfs and Wilson (2003). In the case of extended sources ($\Omega_S > \Omega_{mb}$) the ratios were corrected for the main beam filling factor, which was approximated as $f_{mb} = \Omega_S / (\Omega_S + \Omega_{mb})$. The beams, as well as the source structures, were assumed to be gaussians.

The source sizes reported in Table 1 were estimated from high resolution maps available in the literature. For NGC 3079 a source size of $15'' \times 7.5''$ was estimated for the CO 1–0 emission, considering only intensities above 15% of the peak integrated intensity of the contour map presented by Koda et al. (2002). In NGC 1068 most of the CO 1–0 emission emerges from the two spiral arms, with the largest extension of $\sim 40''$ (e.g. Helfer & Blitz 1995, Schinnerer et al. 2000). Considering intensities above 20% of the peak emission of the high resolution map by Schinnerer et al. (2000) the source size of the CO 1–0 emission in NGC 1068 was estimated as $30'' \times 30''$. For NGC 2623 a source size of $8'' \times 8''$ was estimated from the CO 1–0 map presented in Bryant et al. (1999), which agrees well with the estimate made by Casoli et al. (1988).

In the case of NGC 1365 the CO emission is concentrated in the nuclear and bar regions (Sandqvist et al. 1995). Hence the source size of the CO emission was estimated as $50'' \times 50''$, corresponding to intensities above 20% of the peak emission in the CO 3–2 map by Sandqvist (1999).

From Papadopoulos & Allen (2000) and Davies et al. (2004) the source size of the CO emission in NGC 7469 was estimated as $8'' \times 8''$, which correspond to intensities above 40% of the peak emission in the high resolution map by Davies et al. (2004). The criteria of selection of the source size of CO varies depending on the gradient of the emission observed in the different sources.

The source size of the high density tracers CN, HCN and HNC were estimated through HCN maps available in the literature. In all these maps, we observed that the HCN 1–0 emissions emerge mainly from the nuclear region of the galaxies. Since there are no published maps of CN nor HNC emissions for the galaxies studied here, the corresponding source sizes were considered equal to that of the HCN emission, due to their chemical link. Since there are no HCN maps for NGC 1365 and NGC 2623, the factor $\sqrt{\Omega_S(\text{HCN})} / \sqrt{\Omega_S(\text{CO})} \approx 0.33$ found in NGC 1068 was used to estimate the source size of the HCN 1–0 emission, based on their corresponding $\Omega_S(\text{CO})$. The estimated $\Omega_S(\text{HCN})$ are shown in Table 1.

The line ratios were computed assuming an error of 10% in the reported beam efficiencies η_{mb} , 5% of error in the main beam θ_{mb} (Table 2), and a 10% error in the estimated source sizes θ_S (Table 1). The obtained ratios are shown in Table 8. From these ratios we can conclude that CO, as well as the high density tracers - CN, HCN and HNC - are subthermally excited.

Table 7. Velocity-integrated intensities ^a.

Galaxy	$I(\text{CO})$ 1-0	$I(\text{CO})$ 2-1	$I(\text{CN})$ 1-0	$I(\text{CN})$ 2-1	$I(\text{HCN})$ 1-0 ^b	$I(\text{HCN})$ 3-2	$I(\text{HNC})$ 1-0	$I(\text{HNC})$ 3-2
NGC 3079	205.8±20.6	375.4±37.6	2.7±0.4	4.5±0.7	5.7±0.8	8.0±1.4	2.9±0.5	5.0±1.9
NGC 1068	113.7±11.4	203.6±20.5	9.4±1.0	6.1±0.7	10.0±1.7	22.7±2.5	3.2±0.5	3.5±0.6
NGC 2623	30.2±3.2 ^c	-	≤1.3 ^c	-	-	≤0.5	0.9±0.3 ^c	1.8±0.4
NGC 1365	122.3±12.3	181.0±18.1 ^d	5.9±0.7	7.5±0.9	6.0±0.1	15.0±2.0	4.7±0.6	-
NGC 7469	25.6±3.8 ^e	61.5±6.4	1.8±0.3 ^c	-	1.5±0.3	-	1.1±0.2 ^c	≤0.8

- a) The values refer to the main-beam brightness temperature, I_{mb} , in [K km s⁻¹]. The errors and upper limits correspond to 1σ (defined by the r.m.s. in the spectra) and added in quadrature to the 10% of error considered for the main beam efficiencies, η_{mb} , reported in Table 2 and by the Onsala Space Observatory (OSO).
- b) HCN 1–0 integrated intensities reported by Curran et al. (2000) corrected for a main-beam efficiency of 0.65, according to the on-line values reported by OSO. Our own data are reported for NGC 3079.
- c) Integrated intensities reported by Aalto et al. (2002). The values were rounded to one decimal figure and corrected by the main beam efficiencies reported by OSO, 0.64, 0.45 and 0.43, of the $J=1-0$ transition of HNC, CN and CO, respectively.
- d) CO 2–1 integrated intensity obtained by Sandqvist et al. (1995). A 10% of error was assumed for the reported intensity.
- e) CO 1–0 integrated intensity derived from Curran et al. (2000) considering a main beam efficiency of 0.43 according to the values reported by OSO.

4. Discussion

4.1. The distribution of dense gas

We compare the spectral shape of the high density tracers with HCN and CO position-velocity maps available in the literature in order to address the location of the dense gas.

4.1.1. NGC 1068

In NGC 1068 the two outer peaks of the CO 1–0 spectrum (Figure 1) coincide with the maximum double peak emission seen in the CO position-velocity (p - v) map obtained by Helfer & Blitz (1995), so they can be attributed to the emission emerging from the spiral arms. The center is attributed to the emission emerging from the CND, as can be inferred from the CO 2–1 spectrum (Figure 1). This center peak coincides with the maximum HCN emission at 1100 km s⁻¹ seen in the HCN p - v map obtained by Tacconi et al., (1994). This p - v map is shown in the *left panel* of Figure 5 for comparison, along with the corresponding scaled spectra observed in NGC 1068.

The main spingroup of the CN 1–0 line (Figure 1) shows a shape similar to that of the CO 1–0 line. So contributions of emission coming from the CND, as well as from the spiral arms,

can also be inferred. The main spingroup of the CN 2–1 spectrum also coincides with the maximum HCN emission around 1100 km s⁻¹.

The HCN spectra seem to contain two components, although we fit only one gaussian to the spectrum. The main component fits the region in the p - v where the strongest HCN emission is coming from. The secondary component might be attributed to the secondary peak emission of HCN, observed around 1035 km s⁻¹. Another smaller peak is seen in the p - v map around 1255 km s⁻¹, but this component is not detected in the HCN spectra.

In the HNC spectra, instead, two clear components are observed. The main component has a center velocity of 1073 km s⁻¹ which lies in between the two main peaks of the HCN emission observed in the corresponding p - v map. With respect to the CO p - v map (Helfer & Blitz 1995), the main HNC component comes from a region where the CO emission is faint. Instead, the secondary component of HNC seems to emerge from a region around 1250 km s⁻¹, which corresponds to the secondary peak emission in the CO p - v map, and roughly to the third peak of the HCN emission in the respective map. Although, the latter is uncertain due to the noise in the spectra.

4.1.2. NGC 1365

On top of the *middle panel* of Figure 5 we show the CO 3–2 p - v map of the central region of NGC 1365, from Sandqvist (1999). The spectra below correspond to the re-scaled spectra shown in Figure 2. The double peak structure of the spectra coincides fairly well with the double peak emission observed in the p - v map. The left components of the spectra seem to emerge from a region around 1530 km s⁻¹.

The right components of most of the spectra could emerge from the region around 1710 km s⁻¹, with the exception of the CN 1–0 line. The right component of CN 1–0 seems to emerge from around 1750 km s⁻¹ which, in turn, coincides with the maximum emission level of the right peak in the CO 3–2 p - v map.

The two peaks in the CO 3–2 p - v map are of about the same intensity, which is reflected in the ¹²CO 1–0 spectrum, where both components have intensities $T_A^* \sim 0.3$ K. The ¹²CO 3–2 and ¹³CO 1–0 data obtained by Sandqvist (1999) also have this feature. However, the CN, HCN and HNC spectra, exhibit a gradient between the intensities of their high and low velocity components. This can also be seen in the HCN 1–0 and HCO⁺

Table 8. Line intensity ratios.

Galaxy	CO $\frac{2-1}{1-0}$	CN $\frac{2-1}{1-0}$	HCN $\frac{3-2}{1-0}$	HNC $\frac{3-2}{1-0}$
NGC 3079	0.77±0.20	0.48±0.15	0.18±0.06	0.25±0.12
NGC 1068	0.81±0.21 ^a	0.19±0.05	0.47±0.14	0.15±0.05
NGC 2623	^b	-	-	0.36±0.15
NGC 1365	0.84±0.12 ^c	0.44±0.12	0.42±0.12	-
NGC 7469	0.97±0.28	-	-	≤ 0.20

- a) For NGC 1068 we corrected the JCMT CO $J=2-1$ observations to the beam size of the SEST CO $J=1-0$ line, applying the factor 20/44, the ratio between the respective beams. With this, the beam dilution effect is cancelled in both transition lines.
- b) See Casoli et al. (1988).
- c) For NGC 1365 we also corrected the CO $J=2-1$ observations to the beam size of the CO $J=1-0$ line, applying the factor 25/44 between the respective SEST beams. The ratio given above is slightly higher than the one reported by Sandqvist et al. (1995).

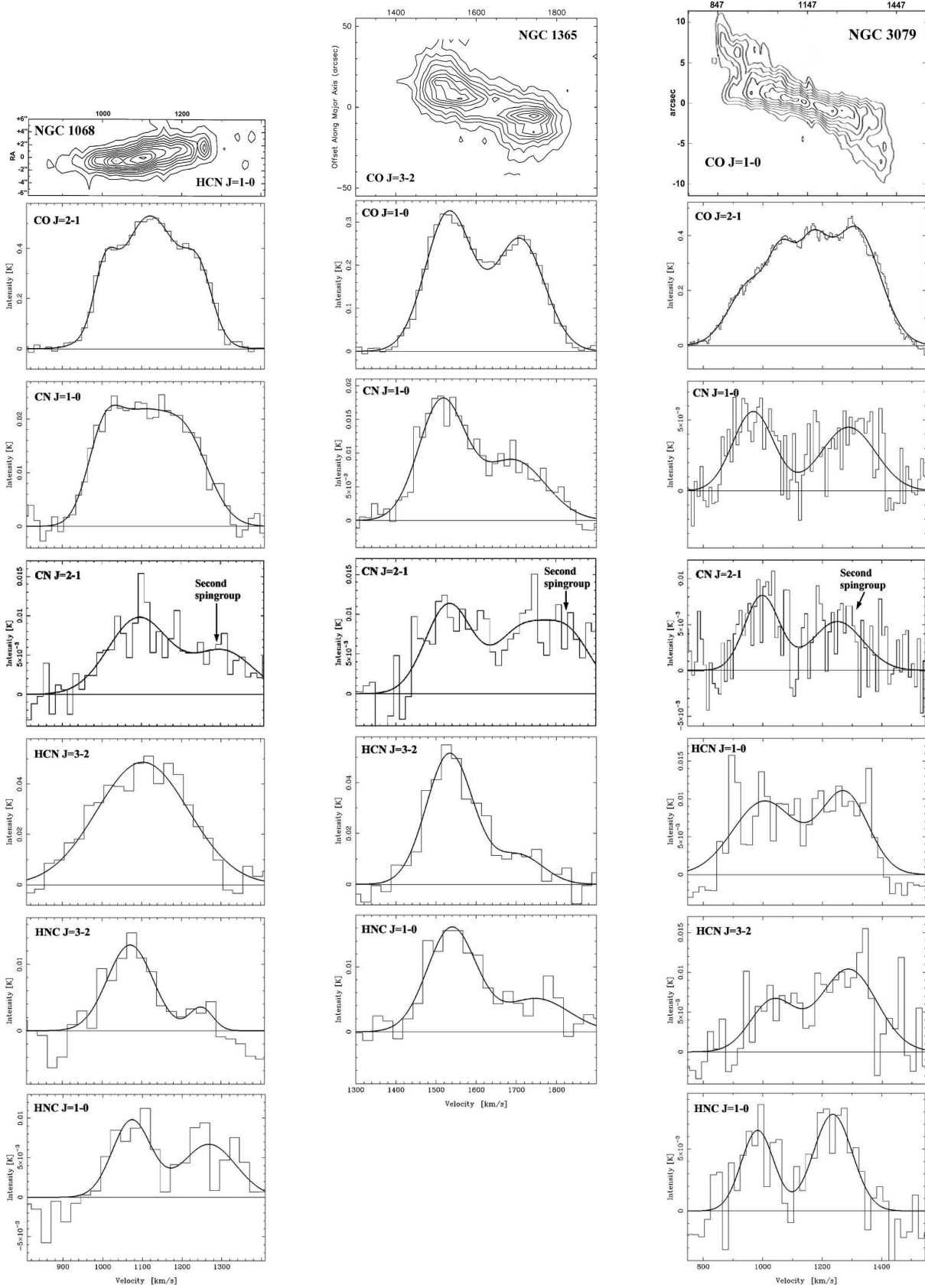


Fig. 5. (Top-left panel) Position-velocity (p - v) map of HCN 1–0 emission in **NGC 1068**, adapted from Tacconi et al. (1994). The spectra below are the respective emission lines of Figure 1, re-scaled to fit the velocity scale of the HCN p - v map. (Top-middle panel) Position-velocity map of CO 3–2 emission in **NGC 1365**, adapted from Sandqvist (1999). The spectra below are the re-scaled versions of the ones shown in Figure 2. (Top-right panel) Position-velocity map of CO 1–0 emission in **NGC 3079**, adapted from Koda et al. (2002). The spectra below are the re-scaled versions of the ones shown in Figure 3.

1–0 spectra obtained by Sandqvist (1999). This intensity gradient could be due to either a larger abundance of the species, or to a higher excitation in the corresponding region of the lower velocities.

Since the observed double peak structure does not change with the beam size (one single feature), we think that the nucleus of NGC 1365 lacks a circumnuclear disk, i.e., it is consistent with a Seyfert 1 nucleus.

4.1.3. NGC 3079

The four-peak structure observed in NGC 3079 can be identified in the CO 1–0 p - v map of Koda et al. (2002). The *top-right* panel of Figure 5 shows an adaptation of the Fig.10 in Koda et al. (2002) with 0'' offset along the minor axis of NGC 3079. Since this galaxy is almost edge-on, most of the CO emission is probably coming from the spiral arms, besides the nuclear region. Instead, the high density tracers are expected to be mostly nuclear, as in the case of NGC 1068. This can explain the double-peak structure of the line shape of the CN, HCN and HNC molecules, in contrast to the CO lines.

Note that in this case the CN spectra are slightly dominated by the lower-velocity peak, as in the case of NGC 1068 and NGC 1365, whereas the HCN and HNC spectra of NGC 3079 are dominated by the higher-velocity peaks. The lower and higher velocity peaks are not perfectly aligned. The maximum separation between the peaks is $\sim 80 \text{ km s}^{-1}$ for the lower-velocity peaks and $\sim 60 \text{ km s}^{-1}$ for the higher-velocity peaks. The lower-velocity peaks are centered around 1000 km s^{-1} and the higher-velocity peaks around 1270 km s^{-1} , which means the high density tracers tend to avoid the peaks of the CO 2–1 emission.

Since the line shapes of CN, HCN and HNC are similar, and they do not change with the beam size, their emissions likely emerge from the nuclear region in this galaxy, in contrast to the case of NGC 1068, where the line shape of the HCN emission changes with the beam size.

4.2. The HCN/HNC line ratios

NGC 1068: The HCN/HNC 3–2 & 1–0 line intensity ratios increase towards the CND. The ratio varies from ~ 2.0 for the lower transition lines, to ~ 6.5 for the higher transition. The large $J=1-0$ beam picks up emission from both the CND and the starburst ring, whereas the $J=3-2$ beam picks up emission coming mainly from the CND. This could be interpreted either as that the abundance ratio differs between the starburst ring and the CND, or that the abundance is actually the same but the physical conditions are different in these two regions. On the other hand, there could also be optical depth effects since the difference in the ratios is consistent with a larger optical depth in the $J=1-0$ transition line of HNC. In section 4.3.1 we estimate the excitation conditions of HCN and HNC, from which we can derive the corresponding optical depths. As described in Figure 6, the optical depth of the $J=1-0$ line of HNC is larger (starting from $\tau=0.01$) than that of the $J=3-2$ line (which starts from $\tau=0.003$) in almost all the possible excitation conditions. In the case of HCN, the situation is the opposite. The lowest optical depth of the HCN $J=1-0$ line is 0.03, whereas in the $J=3-2$ line is 0.32. In any case, $X[\text{HCN}]/X[\text{HNC}]$ is at least 6.5 in the CND. According to Meijerink et al. (2007), this ratio can be found in gas of density $n_{\text{H}} \sim 10^5 \text{ cm}^{-3}$ and with PDR conditions, at a distance from the source of $\sim 10^{16} \text{ cm}$, if the

Habing flux G_0 is about 10^4 , or at a slightly larger distance of $2 \times 10^{16} \text{ cm}$, if $G_0 = 10^5$. On the other hand, in an XDR environment, this ratio would be found at a distance of $7 \times 10^{16} \text{ cm}$, if the radiation flux F_{FUV} is $16 \text{ erg cm}^{-2} \text{ s}^{-1}$, or at a much larger distance of about $2 \times 10^{18} \text{ cm}$, if $F_{\text{FUV}} = 160 \text{ erg cm}^{-2} \text{ s}^{-1}$.

NGC 3079: The HCN/HNC ratio decreases for the higher transitions. The HNC 3–2 emission rivals that of HCN, making the HCN/HNC 3–2 line ratio only 1.6. As described above, a similar analysis of the expected distribution of these ratios and molecules, in a PDR and XDR environments, can be done based on Meijerink et al. (2007).

NGC 2623: In this galaxy we do not detect HCN 3–2. We estimate an upper limit of 0.26 for the HCN/HNC ratio of the $J=3-2$ line. We observe that the ratio does not only decreases for the higher transitions, but also this is the only galaxy in our sample where $I(\text{HCN}) < I(\text{HNC})$ in the $J=3-2$ line, which makes it comparable to galaxies like Arp 220, Mrk 231 and NGC 4418, according to the recent work by Aalto et al. (2007). They propose that the overluminous HNC can be explained by a pumping effect due to mid-IR background radiation with brightness temperatures $T_{\text{B}} \gtrsim 50 \text{ K}$ and densities below critical, or due to the ISM chemistry being affected by X-rays. According to Schilke et al. (1992), shocks are also possible sources of explanation.

The HCN/HNC 1–0 ratio is about 2.0 in NGC 1068 and NGC 3079, and ~ 1.4 in the others. This indicates a brighter HNC emission in NGC 2623, NGC 1365 and NGC 7469. Luminous HNC in galaxies may have the following plausible explanations:

a) **Large masses of hidden cold gas and dust.**

If the HCN and HNC emission is emerging from gas of densities $n(\text{H}_2) > 10^5 \text{ cm}^{-3}$ then the HNC chemistry would be dominated by reactions like $\text{HNC} + \text{O} \rightarrow \text{CO} + \text{NH}$ which would destroy HNC at higher temperatures. Thus, at high gas densities, a bright HNC line would imply a considerable amount of cold ($T_{\text{k}} < 24 \text{ K}$) dense gas.

b) **Chemistry dominated by ion-neutral reactions.**

If, however, the bulk of the HCN and HNC emission is emerging from gas of densities $\sim 10^4 \text{ cm}^{-3}$ then the relative HNC abundance may be substantial, despite the high temperature. The reason for this is that, at lower densities, reactions with HCNH^+ (HCN and HNC reacts with H_3^+ to form HCNH^+) become more important. The ion abundance is higher and once HCN and HNC become protonated, HCNH^+ will recombine to produce either HCN or HNC with 50% probability. This scenario is interesting since the electron and ion abundance is likely higher in PDRs Photon Dominated Regions (PDRs) (Tielens & Hollenbach, 1985). Therefore, in a PDR chemistry, the connection between HNC and kinetic temperature may be weak since we expect the HCNH^+ reactions to be important.

c) **Chemistry dominated by hard X-rays.**

The X-ray irradiation of molecular gas leads to a so called X-ray dominated region (XDR) (e.g. Maloney et al. 1996) similar to PDRs associated with bright UV sources. The more energetic (1–100 keV) X-ray photons penetrate large columns ($10^{22} - 10^{24} \text{ cm}^{-2}$) of gas and lead to a different ion-molecule chemistry. Models of XDRs by Meijerink & Spaans (2005) and Meijerink et al. (2007) indicate that the HNC/HCN column density ratio is elevated (and larger than unity) com-

Table 9. Intensity ratios between the high density tracers.

Galaxy	$\frac{\text{HCN}}{\text{HNC}} \text{ 1-0}$	$\frac{\text{HCN}}{\text{HNC}} \text{ 3-2}$	$\frac{\text{CN}}{\text{HNC}} \text{ 1-0}$	$\frac{\text{CN 2-1}}{\text{HNC 3-2}}$	$\frac{\text{CN}}{\text{HNC}} \text{ 1-0}$	$\frac{\text{CN 2-1}}{\text{HNC 3-2}}$
NGC 3079	2.15±0.67	1.60±0.75	0.64±0.20	1.25±0.58	0.30±0.09	0.78±0.25
NGC 1068	2.01±0.65	6.48±1.95	1.98±0.58	2.58±0.78	0.98±0.29	0.40±0.29
NGC 2623	1.4 ^a	≤0.26	≤0.77 ^a	-	≤0.5 ^a	-
NGC 1365	1.35±0.37	-	0.87±0.25	-	0.64±0.17	0.67±0.19
NGC 7469 ^b	1.50±0.57	-	0.85±0.28	-	0.57±0.21	-

a) Ratios reported by Aalto et al. (2002).

b) New ratios computed using the HCN 1-0 source size estimated from (Davies et al. 2004).

pared to PDRs and quiescent cloud regions for gas densities around 10^5 cm^{-3} .

d) HNC enhanced through mid-IR pumping.

Both HCN and HNC may be pumped by an intense mid-IR radiation field boosting the emission also from low density regions where the lines would not be collisionally excited. For HNC the coupling to the field is even stronger than for HCN, thus increasing the probability for IR pumping in extreme galaxies, such as Mrk 231. Ultraluminous galaxies, such as Mrk 231 and Arp 220, have central mid-IR sources with optically thick radiation temperatures well in excess of those necessary to pump the HNC molecule (Soifer et al. 1999). Even if the HNC abundance is lower than HCN, the HNC emission may have a higher filling factor due to the IR pumping (i.e. IR pumped emission from gas clouds otherwise at too low density to excite the HNC molecule) (e.g., Aalto et al. 2002).

The study carried out so far allows us to distinguish between the above scenarios in some of the sources presented here. The number density $n(\text{H}_2)$ required for alternative (b) is too low to efficiently excite the HNC (or HCN) 1–0 and 3–2 lines, and we should therefore expect subthermal HCN and HNC excitation in this case. An HNC 3–2/1–0 line ratio of 0.3 or less is an indication that the gas densities are below 10^5 cm^{-3} , depending on temperature and column density, as it is discussed in section 4.3. A HNC 3–2/1–0 ratio lower than 0.3 is observed in NGC 3079, NGC 1068 and NGC 7469 (Table 8).

The ratio ~ 0.4 found in NGC 2623 is in the limit between case (a) and (b). On the other hand, case (c) and (d) cannot easily be ruled out. More information is required in order to distinguish between the proposed scenarios, as suggested by Aalto et al. 2007.

The HCN 3–2/1–0 line ratio is below 0.3 only in NGC 3079, whereas it is larger than 0.4 in NGC 1068 and NGC 1365. This result is interesting since it implies that in NGC 3079 both HCN and HNC emission emerge from the same gas, whereas in NGC 1068 the HNC emission has to emerge from a lower ($< 10^5 \text{ cm}^{-3}$) density gas than HCN. It would be interesting to see if this result holds for NGC 1365. We expect to obtain the HNC 3–2 data for this galaxy in a future project.

The pumping scenario (c) should lead to a HNC 3–2/1–0 line ratio close to unity. This is not observed either in the HNC or in the HCN data we have. However, it is not possible to rule out this scenario since low excitation may be the result of mid-IR pumping of low density gas. Detailed modelling is needed in this case.

4.3. Excitation conditions of HCN and HNC

We used the radiative transfer code RADEX¹ (Van der Tak et al. 2007) to explore a wide range of possible excitation conditions that can lead to the observed line ratios. This code is sensible to the column density of a molecule per line width, and uses a constant temperature and density of the collision partner, which in this case is H_2 . Another limitation of RADEX is that it cannot handle large optical depths ($\tau < 100$). Our analysis is not depth dependent and we assume a homogeneous sphere for the escape probability approach. Hence, our models aim to reproduce a sort of average cloud that represent the physical conditions of the emitting gas, which is a well fitted starting model for single dish observations, where all the emissions detected are convolved with the telescope beams.

The grid consists of densities between 10^4 and 10^7 cm^{-3} , temperatures between 4 and 200 K, and column densities per line width between 10^{10} and $10^{18} \text{ cm}^{-2} \text{ km}^{-1} \text{ s}$. Excitation maps were generated in order to obtain the total column density per line width ($N/\Delta\nu \text{ cm}^{-2} \text{ km}^{-1} \text{ s}$) as function of the kinetic temperature (T_k K) and the number density of molecular hydrogen ($n(\text{H}_2) \text{ cm}^{-3}$). The contour lines of the maps describe the dichotomy between temperature and density. This means that, for a given column density, the observed 3–2/1–0 line ratio can be obtained with high temperatures and low densities, or low temperatures and high densities.

The hyperfine structure of the HCN $J=1-0$ transition line is not included in this study. The extrapolated HCN data of the LAMDA² database were used instead (Schöier et al. 2005). Note that the hyperfine components may be overlapping and may interact radiatively in AGN-like environments. This process requires further analysis and modelling that is not included in RADEX. We are not able to generate an excitation map of CN due to the lack of collision data for this molecule. Although, an study to extrapolate the collision data for CN from other known molecules (e.g. CS) is ongoing.

4.3.1. NGC 1068

Figure 6 shows the excitation condition maps for the HCN and HNC molecules, modeled from the average ratios observed in NGC 1068. These maps show that HCN (*top*) requires higher density gas and higher column density than HNC (*middle*) in order to obtain the observed 3–2/1–0 line ratios.

Considering a kinetic temperature $T_k = 80 \text{ K}$ and a density $n(\text{H}_2) \sim 10^5 \text{ cm}^{-3}$, as estimated by Tacconi et al. (1994), we found that $N(\text{HCN})/\Delta\nu \sim 1.5 \times 10^{14} \text{ cm}^{-2} \text{ km}^{-1} \text{ s}$, which agrees with the respective value found by Tacconi et al.

¹ <http://www.sron.rug.nl/~vdtak/radex/index.shtml>

² <http://www.strw.leidenuniv.nl/~moldata/>

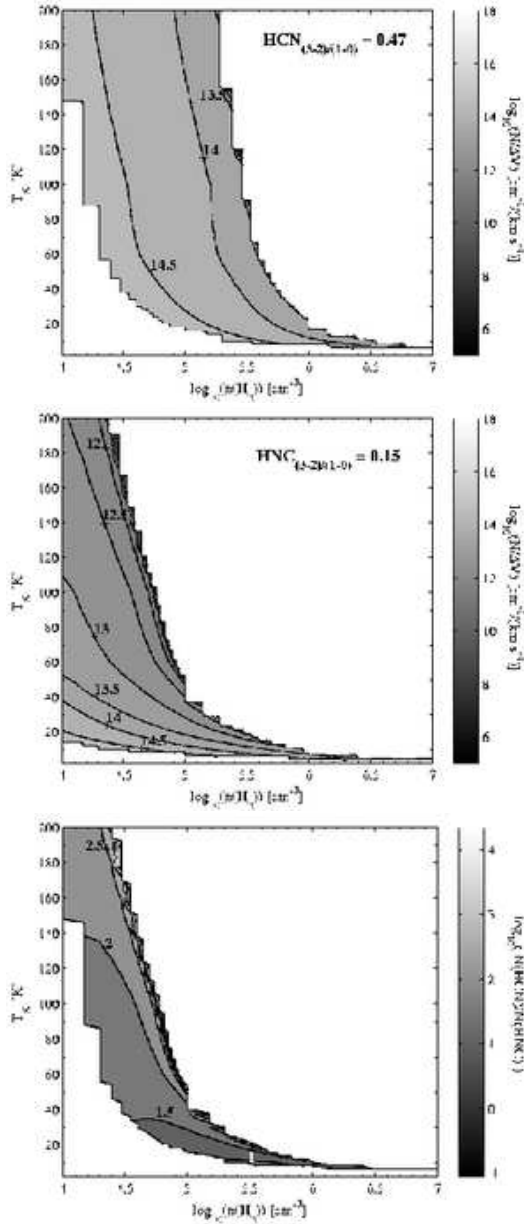


Fig. 6. Excitation conditions modelled for the 3–2/1–0 line ratios of HCN (*top*) and HNC (*middle*) observed in NGC 1068. The conditions required for the HCN and HNC molecules overlap in a narrow region. The relative column densities in the overlap zone of the excitation conditions of these molecules is shown in the *bottom* plot. The optical depth in the whole region explored for HCN ranges between 0.03 and 10 in the $J=1-0$ line, and between 0.32 and 30 in the $J=3-2$ line. In the case of HNC the optical depth ranges between 0.01 and 30 in the $J=1-0$ line, and between 0.003 and 30 in the the $J=3-2$ line. The optically thin limit of both molecules and lines is depicted by the right edge of the excitation conditions, whereas the optically thick limit correspond to the left edge of the figures above.

According to the recent PDR and XDR models by Meijerink & Spaans (2005) and Meijerink et al. (2007), under PDR conditions a temperature $T_k = 80$ K can be reached at a total column density of $N_H \approx 3 \times 10^{21} \text{ cm}^{-2}$, if the Habing flux is $G_0 \sim 10^3$ (a Habing flux $G_0 = 1$ corresponds to a far UV flux $F_{FUV} = 1.6 \times 10^{-3} \text{ erg cm}^{-2} \text{ s}^{-1}$), or at $N_H \approx 8 \times 10^{21} \text{ cm}^{-2}$ if $G_0 \sim 10^5$.

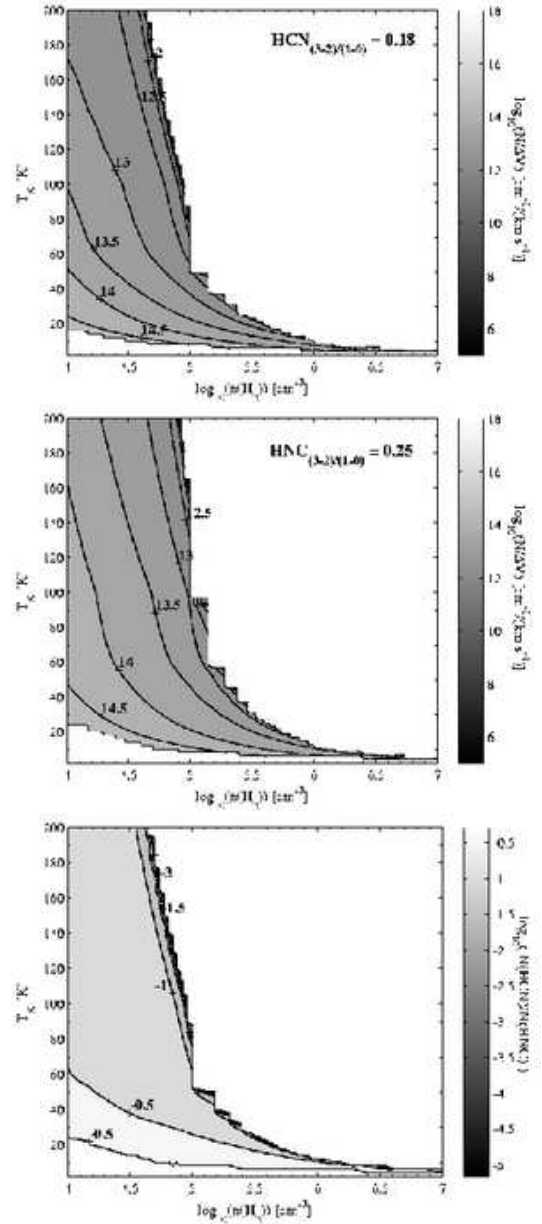


Fig. 7. Excitation conditions modelled for the 3–2/1–0 line ratios of HCN (*top*) and HNC (*middle*) observed in NGC 3079. The excitation conditions required for these molecules overlap in most of the range explored. This suggest that their emissions emerge from gas with the same physical conditions. The *bottom* plot shows the overlap zone. There is a large zone of excitation conditions where the column density of HNC is between 3 and 10 times larger than that of HCN. The contour lines of -0.5 depict the zone of the physical conditions for which the column density of HNC is about 3 times larger than that of HCN. For both molecules and transition lines the optical depth ranges between 0.001 and 30. The optically thick limit is basically defined by the limit of convergence of RADEX ($\tau_{\text{max}} \sim 100$).

At those depths the density $n(\text{H}_2)$ would be slightly higher than 10^5 cm^{-3} , though. On the other hand, in an XDR environment a temperature of 80 K and a density of 10^5 cm^{-3} can be reached at a slightly larger column density of $N_H \approx 10^{22} \text{ cm}^{-2}$, if the impinging radiation field is $F_{FUV} \sim 1.6 \text{ erg cm}^{-2} \text{ s}^{-1}$, or at a much

larger depth equivalent to $N_H \approx 2 \times 10^{24} \text{ cm}^{-2}$ if the radiation flux is $F_{FUV} \sim 160 \text{ erg cm}^{-2} \text{ s}^{-1}$.

However, at a temperature of 80 K and density of 10^5 cm^{-3} there is no solution for HNC. This means that either the HNC emission arises from a gas with different physical conditions than HCN, or that both molecules trace a cooler ($T_k < 80 \text{ K}$) and lower density gas ($n(\text{H}_2) < 10^5 \text{ cm}^{-3}$), if the emission of both molecules arise from the same gas.

If the HCN and HNC emissions actually trace the same gas, the range of possible excitation conditions can be constrained to the zone where the conditions for HCN and HNC overlap. The *bottom* plot of Figure 6 shows the average overlap zone, where the contours correspond to the ratio between the total column densities of HCN and HNC. The overlap zone is defined by the optically thin limit (right edge of the excitation maps) of the HNC transition lines and the optically thick limit (left edge of the excitation maps) of the HCN lines. The models show that $N(\text{HCN})$ is larger than $N(\text{HNC})$ in all the overlap zone. According to Figure 10 in Meijerink & Spaans (2005), $N(\text{HNC})/N(\text{HCN})$ column density ratios lower than unity can be found mostly in PDRs, but also in XDR environments if the total column density $N(\text{H})$ is lower than 10^{24} cm^{-2} . If we still assume the same temperature (80 K) proposed by Tacconi et al. (1994), and we consider the contour line where $N(\text{HCN})$ is about 2.5 orders of magnitude larger than $N(\text{HNC})$, we find that the gas density should be $n(\text{H}_2) \sim 6 \times 10^4 \text{ cm}^{-3}$, which agrees with the observed HNC 3–2/1–0 line ratio discussed in section 4.2. However, this density would not be consistent with the result found by Tacconi et al. (1994) nor with the observed HCN 3–2/1–0 line ratio, which implies that the HNC emissions arise from a more diffuse gas than HCN.

4.3.2. NGC 3079

In contrast to NGC 1068, the excitation conditions modelled for the HCN and HNC line ratios observed in NGC 3079, overlap in most of the range explored (Figure 7). This suggest that the emission from both molecules likely arise from the same gas. The spectral line shapes of HCN and HNC, showed in Figure 3, also hint that their distribution may be the same, although their line centers and widths are affected by noise. The *bottom* plot of Figure 7 shows the overlap zone of the excitation conditions. In most of these conditions $N(\text{HNC})$ is between 0.5 and 1 order of magnitude larger than $N(\text{HCN})$.

According with the PDR and XDR models by Meijerink & Spaans (2005), a column density ratio $N(\text{HNC})/N(\text{HCN})$ larger than unity can be found only in XDR environments at a total column density $N(\text{H}) > 10^{24} \text{ cm}^{-2}$, with radiation fields F_x of about $1.6 \text{ erg cm}^{-2} \text{ s}^{-1}$ (or equivalent Habing flux $G_0 \sim 10^3$) and total density $n(\text{H}) \sim 10^3 \text{ cm}^{-3}$. $N(\text{HNC})/N(\text{HCN})$ column density ratios larger than unity at $N(\text{H}) > 10^{24} \text{ cm}^{-2}$ can also be found with stronger radiation fields ($F_x \sim 160 \text{ erg cm}^{-2} \text{ s}^{-1}$) and higher densities ($n(\text{H}) \sim 3 \times 10^5 \text{ cm}^{-3}$). On the other hand, $N(\text{HNC})/N(\text{HCN})$ can be larger than unity at $N(\text{H}) < 10^{23} \text{ cm}^{-2}$ if the radiation fields are on the order of $1.6 \text{ erg cm}^{-2} \text{ s}^{-1}$ and the total density is about $3 \times 10^5 \text{ cm}^{-3}$.

In our models we did not explore densities lower than 10^4 cm^{-3} since the HCN and HNC molecules are expected to trace higher densities. If we assume a kinetic temperature of 80 K, as in the case of NGC 1068, and a density $n(\text{H}_2) \sim 10^5 \text{ cm}^{-3}$, the column densities per line width would be about 10^{12} and $10^{13} \text{ cm}^{-2} \text{ km}^{-1} \text{ s}$ for HCN and HNC, respectively. In the case of HNC both transition lines are equally optically thick at 80 K in the whole range of densities, whereas HCN is more optically

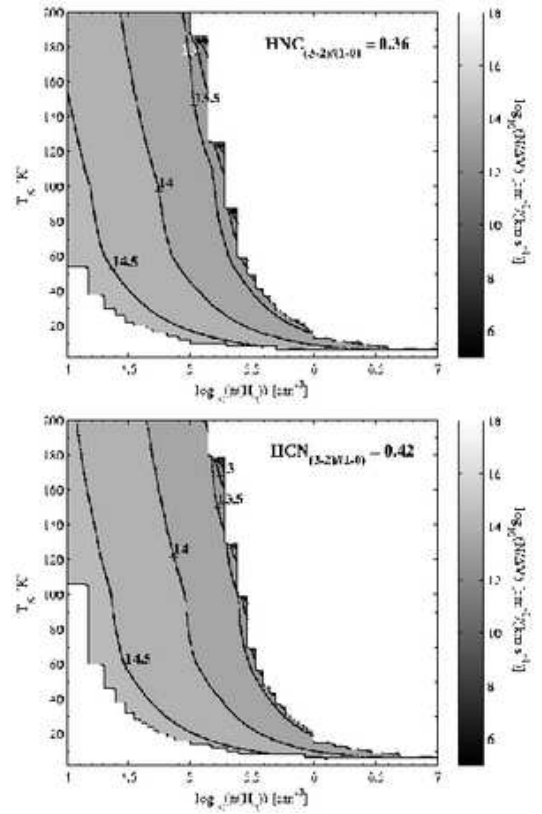


Fig. 8. Excitation conditions modelled for the 3–2/1–0 line ratio of HNC (*top*) and HCN (*bottom*) observed in NGC 2623 and NGC 1365, respectively. For NGC 2623 the optical depth of HNC 3–2 ranges between 0.003 and 10 in the $J=1-0$ line, and between 0.32 and 30 in the $J=3-2$ line. In the case of NGC 1365 the optical depth in the HCN 3–2 line ranges between 0.1 and 30, and between 0.01 and 10 in the $J=1-0$ line.

thin. At a density of 10^5 cm^{-3} the optical depth of HNC is ~ 1 in both lines, whereas τ is ~ 0.3 and ~ 0.1 in the $J=1-0$ and $J=3-2$ lines of HCN, respectively. A density lower than 10^5 cm^{-3} is more likely to be the right case in order to be consistent with the line ratios observed and discussed in section 4.2.

4.3.3. NGC 2623 and NGC 1365

Both NGC 2623 and NGC 1365 have similar excitation conditions for HNC and HCN, respectively. As in the case of HCN in NGC 1068, both molecules could be embedded in gas with densities larger than 10^5 cm^{-3} at 80 K, which is consistent with line ratios larger than 0.3, as discussed in section 4.2. The column densities per line width of these molecules would be about $6 \times 10^{13} \text{ cm}^{-2} \text{ km}^{-1} \text{ s}$ for HNC and about $10^{14} \text{ cm}^{-2} \text{ km}^{-1} \text{ s}$ for HCN, if the gas density is 10^5 cm^{-3} .

4.4. The CN/HNC and CN/HCN line ratios

The CN/HNC ratio increases towards the CND in both galaxies, NGC 1068 and NGC 3079. The CN/HNC 1–0 ratio is lower than unity in all the galaxies, with the exception of NGC 1068. This can be interpreted as that HNC is more abundant than CN, assuming the same excitation conditions and that the emission emerge from the same gas and distribution in the galaxy. However, since we do not really know the source size of CN (and

basically neither that of HNC) the beam dilution effects could be more (or less) severe than estimated here.

Although the beam dilution uncertainty of CN also applies to the CN/HCN ratio, this case is more interesting because none of the galaxies where we do have data show ratios larger than one, neither for the global ratio ($J=1-0$) nor for the nuclear part of the galaxies (higher transitions). All of these galaxies are considered active galaxies, so the presence of an AGN increases the chances of finding an X-ray dominated region (XDR) in their nuclear regions, as it seems to be the case of NGC 1068, according to Usero et al. (2004).

In an XDR the CN molecule is expected to be more abundant than HCN (e.g., Lepp & Dalgarno 1996, Meijerink & Spaans 2005 and Meijerink et al. 2007), and hence the CN/HCN intensity ratio could also be larger than unity, especially for the higher transition lines - CN 2-1 and HCN 3-2 - where the beam dilution is less important than for the $J=1-0$ line. However, this is not seen in any of the sources presented here, nor in the sample of galaxies shown by Aalto et al. (2002), where results for AGN are presented along with starburst galaxies.

According to Meijerink et al. (2007), in a PDR environment the $N(\text{CN})/N(\text{HCN})$ column density ratio ranges between 2.0 and 0.5 for densities between 10^4 and 10^6 cm^{-3} , respectively, whereas in an XDR this ratio varies from over a 1000 (at $n(\text{H}_2) \sim 10^4 \text{ cm}^{-3}$) to 40 (at $n(\text{H}_2) \sim 10^6 \text{ cm}^{-3}$). If the CN intensity lines are proportional to the column density, and the estimate of the beam dilution is accurate enough, our results would favor a PDR scenario, rather than an XDR, with densities $< 10^6 \text{ cm}^{-3}$ in the central regions of all these galaxies. However, if the CN molecule is indeed more abundant than HCN, then the weaker intensity lines could be also due to a stronger optical depth effect (in the escape probability sense) for CN. A rigorous modeling and analysis of the CN molecule would be required in order to understand and predict the intensities of this molecule.

On the other hand, the PDR scenario would also be consistent with the results found for the HNC and HCN molecules described above. HCN/HNC line intensity ratios larger than unity are usually found in PDR environments at total column densities $N(\text{H})$ lower than 10^{22} cm^{-2} , while this ratio is larger for strong ($> 10 \text{ erg s}^{-1} \text{ cm}^{-2}$) radiation fields and low ($\sim 10^4 \text{ cm}^{-3}$) densities in an XDR environment (Meijerink et al. 2007). The lower densities required to observe this ratios in an XDR environment tend to dismiss this alternative since our simulations in section 4.3 favor densities $\sim 10^5 \text{ cm}^{-3}$ for the HNC and HCN molecules, as in the case of NGC 1068. In particular, there is evidence of recent starburst in the dense nuclear disk of NGC 1068 (Davies et al. 2006). These results are consistent with a model considering both, AGN and starburst components, required for modelling the UV to FIR atomic spectrum of NGC 1068 (Spinoglio et al. 2005).

5. Conclusions

We have used the SEST and JCMT telescopes to carry out a survey of CN 2-1, HCN 3-2 and HNC 3-2 line emission in a sample of 4 Seyfert galaxies, plus NGC 3079 which was observed with the IRAM 30m telescope. The conclusions we draw are as follows:

- 1) We detected HNC 3-2 emission in 3 of the 5 galaxies, while we obtain an upper limit for one of them (NGC 7469). HCN 3-2 was also detected in 3 galaxies (NGC 3079, NGC 1068 and NGC 1365), while it was not detected in NGC 2623. CN 2-1, along with the spingroups ($J = 5/2 - 3/2$, $F = 7/2 -$

$5/2$) and ($J = 3/2 - 1/2$, $F = 5/2 - 3/2$) was also detected in NGC 3079, NGC 1068 and NGC 1365.

- 2) The line shapes observed in NGC 1365 and NGC 3079 suggests that there is no circumnuclear disk in these galaxies.
- 3) We find that in 3 of the galaxies the HNC 3-2/1-0 line ratios suggest that the HNC emissions emerge from gas of densities $n \lesssim 10^5 \text{ cm}^{-3}$, where the chemistry is dominated by ion-neutral reactions. In NGC 2623 a model of large masses of hidden cold (10 K) gas and dust, as well as a chemistry dominated by ion-neutral reactions, are yet to be distinguished as the correct interpretation for the bright HNC observed in this galaxy.
- 4) The 3-2/1-0 line ratios and the modelled excitation conditions imply that the HNC emission emerges from a more diffuse ($n < 10^5 \text{ cm}^{-3}$) gas region than the HCN emission ($n > 10^5 \text{ cm}^{-3}$) in NGC 1068, whereas they emerge from the same lower density ($n \lesssim 10^5 \text{ cm}^{-3}$) gas in NGC 3079.
- 5) The HCN/HNC and CN/HNC line ratios tentatively favor a PDR scenario, rather than an XDR one, in the 3 Seyfert galaxies where we have CN, HNC and HCN data. The $N(\text{HNC})/N(\text{HCN})$ column density ratios obtained for NGC 3079 can be found only in XDR environments.

In order to complete the sample, we plan to observe HCN 3-2 and CN 2-1 in NGC 7469, CN 2-1 in NGC 2623 and HNC 3-2 in NGC 1365. We plan to perform high resolution observations to further study the distribution and source sizes of CN and HNC.

Modeling of the collision data for the CN molecule would be useful to estimate the $N(\text{CN})/N(\text{HCN})$ column density ratio, which would complement the $N(\text{HNC})/N(\text{HCN})$ ratio in order to have a more sophisticated tool to estimate and distinguish the prevalent environment conditions of the high density gas in the nuclear region of Seyfert galaxies.

The AGN contribution (through XDR effects) is typically of a small angular scale and can be seriously affected by beam dilution at the transition lines studied in this work. On the other hand, the starburst contribution is of a larger angular scale than the AGN, and its effects can be contaminating our observations, and hence leading to the favored PDR scenario found with our models. Hence, our suggested interpretations could change if we zoom in on these sources. Therefore, high resolution maps of HNC and CN molecules are necessary to complement those of HCN, and to do a more accurate estimate of molecular abundances and line intensity ratios, which take source size into account. Observations of the higher transition lines (e.g. $J=4-3$) can also aid to disentangle the effects of the AGN and the starburst ring, due to the smaller beam size obtained at higher frequencies.

Acknowledgements. We are grateful to the SEST staff for their help during the observing run. We thank S. Curran and A. Polatidis for help with some of the SEST observations. We are grateful to S. Hüttemeister, M. Spaans, and R. Meijerink for discussions. We also thank F. van der Tak and J. Black for their help and discussions about RADEX. Molecular databases that have been helpful include LAMBDA and NIST.

References

- Aalto S., Polatidis A.G., Hüttemeister S., Curran S.J., 2002, *A&A*, 381, 783 (APHC02)
- Aalto, S., Spaans, M., Wiedner, M.C., Hüttemeister, S., 2007, *A&A*, 464, 193
- Bryant, P.M., 1996, PhD Thesis
- Bryant, P.M., & Scoville, N.Z., 1999, *AJ*, 117, 2632
- Casoli F., Combes F., Dupraz C., Gerin M., Encrenaz P., Salez M, 1988, *A&A*, 192, L17
- Curran, S.J., Aalto, S., & Booth, R.S. 2000, *A&AS*, 141, 193

- Davies R.I., Tacconi L.J. & Genzel, R., 2004, *ApJ*, 602, 148
- Davies, R.I., Genzel, R., Tacconi, L.J., Mueller Sanchez, F., Sternberg, A., 2006, *astro-ph/0612009*
- Graciá-Carpio J., García-Burillo S., Planesas P., & Colina L., 2006, *ApJ*, 604, L135
- Helfer, T.T., & Blitz L., 1995, *ApJ*, 450, 90
- Hirota T., Yamamoto S., Mikami H., Ohishi M., 1998, *ApJ* 503, 717
- Hirota T., Yamamoto S., Kawaguchi, K., Sakamoto, A., Ukita, N., 1999, *ApJ* 520, 895
- Hüttemeister S., Henkel C., Mauersberger R., et al., 1995, *A&A* 295, 571
- Koda J., Sofue Y., Kohno K., Nakanishi H., Onodera S., Okumura S.K., and Irwin J.A., 2002, *ApJ*, 573, 105
- Kohno K., Kawabe R., Shibatsuka T., and Matsushita S., 2000, in *ASP Conf. Ser.*, 217, *Imaging at Radio through Submillimeter Wavelengths*, Mangum J.G. and Radford S.J.E., Eds.
- Kohno K., Matsushita S., Vila-Vilaró B., Okumura S.K., Ishizuki S., Kawabe R., 2001, in *ASP Conf. Ser.*, 249, *The Central Kiloparsec of Starbursts and AGN: The La Palma Connection*, Knapen J.H., Beckman J.E., Shlosman I., and Mahoney T.J., Eds.
- Kohno K., 2005, *AIP Conf. Proc.*, 783, 203, *THE EVOLUTION OF STARBURSTS: The 331st Wilhelm and Else Heraeus Seminar*
- Lepp, S., & Dalgarno, A., 1996, *A&A*, 306, L21
- Maloney, P.R., Hollenbach, D.J. & Tielens, A.G.G.M., 1996, *ApJ*, 466, 561
- Meijerink, R. & Spaans, M., 2005, *A&A* 436, 397 (MS05)
- Meijerink, R., 2006, Ph.D. Thesis
- Meijerink, R., Spaans, M. & Israel, F.P., 2007, *A&A* 461, 793
- Ngeow C. and Kanbur S.M., 2006, *ApJ*, 642, L29
- Nguyen-Q-Rieu, Jackson, J.M., Henkel, C., Truong-Bach, Meuersberger, R., 1992, *ApJ*, 339, 521
- Papadopoulos, P.P. & Allen, M.L., 2000, *ApJ* 537, 631
- Rodríguez-Franco, A., Martín-Pintado, J., Fuente, A., 1998, *A&A*, 329, 1097
- Rohlf K., Wilson T.L., 2003, Springer, 4th Ed., ISBN: 3540403876
- Sandqvist, Aa., Jörsäter, S., Lindblad, P.P., 1995, *A&A*, 295, 585
- Sandqvist, Aa., 1999, *A&A*, 343, 367
- Soifer, B.T., Neugebauer, G., Matthews, K., Becklin, E.E., Ressler, M., Werner, M.W., Weinberger, A.J., Egami, E., 1999, *ApJ*, 513, 207
- Schilke P., Walmsley C.M., Pineau de Forêt G., et al., 1992, *A&A* 256, 595 (S92)
- Schinnerer E., Eckart A., Tacconi L.J., Genzel R., 2000, *ApJ*, 533, 850
- Schöier, F.L., van der Tak, F.F.S., van Dishoeck E.F., Black, J.H. 2005, *A&A* 432, 369
- Solomon P.M., Downes D., Radford S.J.E., 1992, *ApJ*, 387, L55
- Spinoglio, L., Malkan, M.A., Smith, H.A., González-Alfonzo, E., Fischer, J., 2005, *ApJ*, 623, 123
- Tacconi L.J., Genzel R., Blitz M., Cameron M., Harris A.I., Madden S., 1994, *ApJ*, 426, L77
- Tachikawa, H., Iyama, T. and Fukuzumi, T., 2003, *A&A*, 397, 1
- Talbi, D., Ellinger, Y. and Herbst, E., 1996, *A&A*, 314, 688
- Usero A., García-Burillo S., Fuente A., Martín-Pintado J., Rodríguez-Fernández N.J., 2004, *A&A* 419, 897 (U04)
- Van der Tak, F.F.S., Black, J.H., Schöier, F.L., Jansen, D.J., van Dishoeck, E.F., 2007, *A&A* 468, 627
- Wall, W. F., Jaffe, D. T., Bash, F. N., et al., 1993, *ApJ*, 414, 98
- Wild, W., Harris, A. I., Eckart, A., et al. 1992, *A&A*, 265, 447